Nonlinear and chaotic magnetization dynamics near bifurcations of the Landau-Lifshitz-Gilbert equation

Aaron M. Ferona and Robert E. Camley

Center for Magnetism and Magnetic Nanostructures, University of Colorado at Colorado Springs,
Colorado Springs, Colorado 80918, USA

The behavior of a uniformly magnetized domain of ellipsoidal shape subject to a static external field and oscillatory external driving field is analyzed near bifurcation events. The analysis includes the effects of both linear and circularly polarized driving fields and is performed using numerical simulations of the Landau-Lifshitz-Gilbert (LLG) equation. Under a linearly polarized driving field, the LLG equation is a nonautonomous differential equation which can lead to complex magnetization motions, such as bistability, multiperiodic orbits, quasiperiodicity, and chaos. Under a circularly polarized driving field, the LLG equation can be written in autonomous form by transforming to the frame rotating with the driving field. The autonomous nature allows one to perform a fixed-point analysis of the system for select demagnetization factors. Similarities and differences between the driven systems are highlighted through bifurcation diagrams, phase portraits, basins of attraction, and Lyapunov exponents. Magnetization switching, prolonged transients, quasiperiodicity, and chaos are observed with both linearly and circularly polarized driving fields in the magnetic systems investigated.

I. INTRODUCTION

The Landau-Lifshitz-Gilbert (LLG) equation is a phenomenological [1,2] model that describes the behavior of magnetic domains under the influence of an effective magnetic field. In micromagnetics, the effective field is commonly composed of five different domain energy terms: exchange, anisotropy, magnetostatic, external field, and magnetoelastic [1,3–5]. With nonuniform magnetization configurations (spatially varying domains) the LLG equation is coupled to Maxwell's equations and boundary conditions through the effective field due to the long-range dipolar interactions. This micromagnetic construct leads to a large number of coupled nonlinear differential equations where phenomena such as spin waves, eddy currents, and domain-wall formation can be studied [6–8].

In this paper we limit our focus to a single uniformly magnetized domain (macrospin approximation) of ellipsoidal shape with negligible anisotropy, exposed to an external static and oscillatory driving field. Uniform magnetization of a single domain allows one to ignore the exchange interaction with other domains and to express the magnetostatic (demagnetization) field in terms of a demagnetization tensor [3,9,10]. The spatially uniform solutions discussed throughout this paper and other recent works [11–18] provide a foundation for investigating nonlinear and chaotic effects with additional complexities (anisotropy, exchange, spin transfer, etc.). In addition, magnetic recording processes are continuing to scale down to dimensions where spatially uniform solutions might play a prominent role in their operation [3,19–22], and magnetic hyperthermia research [23] on nanoparticles has applications to possible cancer treatments.

This work is motivated by a combination of recent experimental [24–28] and theoretical [29–33] results. It has experimentally been shown that in ultrasmall waveguides one can have large oscillating magnetic fields at microwave frequencies, with amplitudes in the 200 Oe range rather than the 0.1 Oe range usually found in ferromagnetic resonance cavity experiments. By reducing the size of the waveguides

even smaller it is reasonable to expect that oscillating waves with amplitudes of several kOe are possible. Some recent theoretical calculations have explored magnetization dynamics using these large driving fields in spherical nanoparticles [29]. These calculations showed a set of interesting behaviors: (1) One could obtain reversal of the magnetization direction, against the direction of the static magnetic field, by increasing the amplitude of the driving field; (2) there existed a very long-lived transient, at a frequency near the uniform resonance frequency, for driving amplitudes slightly above and below the critical amplitude which causes reversal of the magnetization. These results, however, were preliminary in the sense that they only dealt with spheres and no detailed calculation was given for the critical amplitude.

We note that magnetization reversals are an ongoing topic of interest, in part because of their relevance to magnetic recording. A number of different mechanisms have been investigated both theoretically and experimentally. This includes, for example, magnetization reversals in nanopillars caused by polarized spin currents [34–37] or microwave assisted switching and the related microwave assisted magnetic recording (MAMR) [38,39]. The mechanism discussed here also is particularly suited to nanogeometries because this ensures the single domain behavior. However, the present study is quite different from previous work, particularly MAMR, in that the switching is not accomplished in the presence of an aiding static field, but creates a switching to a new state which has the magnetization opposite to the applied field.

In this paper we significantly extend the earlier [29] calculations. First, we consider a variety of nanostructures: spheres, cylinders, and planes. We present bifurcation diagrams for each type of particle and show how the different particles lead to different results. We then explore the general kinds of dynamics for each nanostructure as a function of the driving field amplitude. The topology of each nanostructure is discussed in terms of attractors and basins of attraction along with their visual aids. We also present a stability analysis to better understand the reversal of the magnetization and

prolonged transient behavior that has been observed in the spherical system.

In Sec. II we present the LLG equation, magnetic configurations, and our methods of finding numerical solutions. Sections III–V explore the parameter space associated with the spherical, long cylindrical, and infinite plane magnetic domain geometries. In Sec. VI we summarize our significant results and conclusions.

II. NUMERICAL ANALYSIS

Numerical simulations of the LLG equation start by putting the equation in dimensionless form. One accomplishes this by measuring the magnetization and effective field in units of M_s ($\boldsymbol{m} = \boldsymbol{M}/M_s$ and $\boldsymbol{h}_{\text{eff}} = \boldsymbol{H}_{\text{eff}}/M_s$) and measuring time in units of $(\gamma M_s)^{-1}$, where $\gamma = 1.84 \times 10^{11} \text{radT}^{-1}\,\text{s}^{-1}$ is the gyromagnetic ratio and $M_s = 2.199$ T is the saturation magnetization (appropriate for iron [40]). The dimensionless LLG equation is given by

$$\frac{d\boldsymbol{m}}{dt} - \alpha\left(\boldsymbol{m} \times \frac{d\boldsymbol{m}}{dt}\right) = -\boldsymbol{m} \times \boldsymbol{h}_{\text{eff}}, \qquad (1)$$

where α, $\boldsymbol{m}$, and $\boldsymbol{h}_{\text{eff}}$ are the dimensionless damping constant, magnetization, and effective magnetic field, respectively. Here, we are treating the LLG equation in the context of monodomain processes or the macrospin approximation. The value of the damping constant is material dependent and typically lies between 0.001 and 0.1 for most ferromagnetic materials. The inclusion of damping in the LLG equation accounts for the many different microscopic energy-loss mechanisms, such as spin waves, eddy currents, phonon's, etc. Applying the dot product of $\boldsymbol{m}$ with Eq. (1) reveals that $\boldsymbol{m}$ is always perpendicular with the change in $\boldsymbol{m}$ (i.e., $\boldsymbol{m} \cdot d\boldsymbol{m}/dt = 0$), and $\boldsymbol{m}$ is normalized such that its modulus is unity. Topologically, these properties of the normalized LLG equation result in the dynamic motion of the magnetization vector $\boldsymbol{m}$ being constrained to the surface of a unit sphere. The effective fields we investigate in this paper are given by

$$\boldsymbol{h}_{\text{eff}} = \boldsymbol{h}_d(t) - N_{11}m_1\hat{\boldsymbol{x}} - N_{22}m_2\hat{\boldsymbol{y}} + (h_s - N_{33}m_3)\hat{\boldsymbol{z}}, \quad (2)$$

where $\boldsymbol{h}_d(t) = h_d \cos(\omega_d t)\hat{\boldsymbol{x}}$ or $\boldsymbol{h}_d(t) = h_d \cos(\omega_d t)\hat{\boldsymbol{x}} + h_d \sin(\omega_d t)\hat{\boldsymbol{y}}$, corresponding to linearly and circularly polarized driving fields perpendicular to the static field $h_s\hat{\boldsymbol{z}}$. The Cartesian components of the demagnetization tensor we consider are $N_{11} = N_{22} = N_{33} = 1/3$, $N_{11} = N_{22} = 1/2$, and $N_{22} = 1$, which correspond to spherical, long cylinder, and infinite plane magnetic domain geometries. The numerical subscripts 1, 2, and 3 correspond to the Cartesian x, y, and z coordinates, respectively. In the absence of damping and an external driving field, one can derive the normal mode frequency

$$\omega_0 = \sqrt{[h_s + (N_{11} - N_{33})][h_s + (N_{22} - N_{33})]} \qquad (3)$$

from Eqs. (1) and (2). For small damping ($\alpha \leqslant 0.1$) and initial magnetizations not very far ($\theta_0 \leqslant \pi/3$) from the equilibrium direction, ω_0 provides an adequate description of the precessional frequency. In this limit, if the magnetization is initially away from the equilibrium it will decay at ω_0 until it is oriented along the equilibrium direction. Similar to the driven pendulum and harmonic oscillator systems,

interesting nonlinear phenomena do not occur unless the driving frequency ω_d is within a few factors of the normal mode frequency ω_0. Therefore, much of our LLG analyses focused on driving frequencies in this regime.

Spherical coordinates are the most natural coordinate representation for the LLG equation due to the fundamental constraint $\boldsymbol{m} \cdot \boldsymbol{m} = 1$. The constraint reduces the state variables to just (θ, ϕ); however, singularities at the poles of the sphere demand one to use a different coordinate representation for numerical analysis. In our numerical analysis we use Cartesian coordinates (probably the most common) and have implemented and compared four different integration schemes: standard fourth-order Runge-Kutta (RK4), explicit Runge-Kutta [41] of order (4)5 (RK45), LSODA [42], and the midpoint method with second-order Adams-Bashforth extrapolation [43] (MP-AB2). The general behavior of $\boldsymbol{m}$ over 10^5 $(\gamma M_s)^{-1}$ (247 ns), using 0.1 $(\gamma M_s)^{-1}$ step sizes yielded almost identical results between MP-AB2, LSODA, and RK45, while RK4 gave nonphysical results after just 20 ns (of course, reducing the step size used in the RK4 method stabilizes the solution). The magnitude of $\boldsymbol{m}$ deviated the least using MP-AB2, where the maximum deviation of $|\boldsymbol{m}(t)| - 1$ was on the order of $\pm 10^{-13}$, over 10^5 $(\gamma M_s)^{-1}$ for a typical simulation. All of the calculations presented in this paper were performed using the MP-AB2 scheme due to its stability and geometric structure preserving properties [43]. The other numerical schemes were occasionally used as sanity checks.

Bifurcations can be identified by structural changes in the phase portrait of a dynamic system as a parameter of the system is varied. Of the free parameters (h_s, h_d, ω_d, and α) that can be varied in the LLG equation we have chosen to analyze bifurcations as we vary the drive amplitude h_d (this is common practice in most driven dynamic systems). The driving frequency ω_d is only varied as we analyze the different domain geometries (demagnetization factors), because the geometry along with the static field determines the normal mode frequency, and we are interested in drive frequencies within a factor of a few from the normal mode frequency. For consistency and comparisons across the various geometric domains we have chosen to fix the frequency ratio ω_d/ω_0 to approximately 3.4. The factor $\omega_d/\omega_0 \approx 3.4$ corresponds to oscillating microwave waveguide frequencies of 1.0, 109.2, and 14.9 GHz for the sphere, cylinder, and thin-film geometries, respectively. At the end of Secs. III–V, we provide a brief discussion of how the bifurcation landscape changes with different frequency ratios. Furthermore, in all calculations presented we have fixed the static field and damping constant to $h_s \approx 0.0045$ (≈ 0.1 kOe) and $\alpha = 0.01$, respectively. The values of our parameter choices are motivated by ferromagnetic resonance experiments, but are mostly arbitrary and may be changed to provide different behaviors. In the following sections, we have chosen to represent our results in the cgs unit system in the hopes that the field strengths and time scale are more familiar to the reader.

III. SPHERICAL DOMAIN

A bifurcation diagram allows one to analyze the long-term periodic behavior of dynamic systems over a range of control
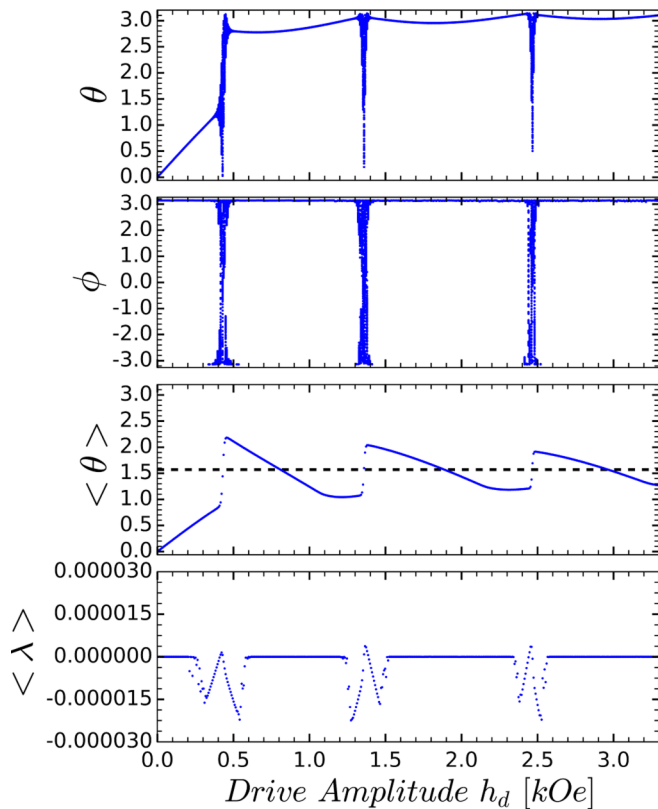
FIG. 1. Bifurcation diagram of the linearly polarized driven spherical domain (top two panels), average value of θ, and the average largest Lyapunov exponent $\langle\lambda\rangle$ as a function of h_d from 1238 to 1337 ns. $N_{11} = N_{22} = N_{33} = 1/3$, $\omega_d = 2\pi$ rad/ns, $\omega_0 = 1.84$ rad/ns, $h_s = 0.1$ kOe, $\alpha = 0.01$, and $(\theta_0 = 0, \phi_0 = 0)$.

parameter values (in our case the drive amplitude). Figure 1 shows a bifurcation diagram of the θ and ϕ coordinates, the average value of θ, $\langle\theta\rangle$, and the average largest Lyapunov exponent (LLE) $\langle\lambda\rangle$ as a function of h_d for the spherical domain driven by a linearly polarized field at $\omega_d = 2\pi$ rad/ns, where $N_{11} = N_{22} = N_{33} = 1/3$ and $\omega_0 = 1.84$ rad/ns. For every drive amplitude (x axis) a complete solution of the LLG equations is found over the time interval of interest. Then one looks at the position of $\boldsymbol{m}$ at discrete time intervals, which for driven systems, is most commonly the drive period. Numerically, this creates a Poincaré or iterated map for the phase-space trajectories and allows one to study various bifurcations.

One can obtain additional insight into the components amplitude of oscillation by choosing to start the Poincaré sections at the peak or maximum of the component oscillations sometime after the initial transients have died out. Figure 1 and the remaining bifurcation diagrams were derived from locating the maximum value of θ and ϕ over one drive period sometime after transients are believed to have died out (we use 1237 ns), then in units of the drive period, find 99 more values of the component. The $\langle\theta\rangle$ describes the abrupt switching behavior at the bifurcation events. The LLE is used to quantify the divergence of two phase-space trajectories that start initially close to one another. This allows one to determine the sensitivity of the system to the initial conditions. In this

paper the average LLE $\langle\lambda\rangle$ is calculated by finding a reference solution for some initial condition (θ_0, ϕ_0); then randomly selecting 16 initial conditions some small distance ($\epsilon \approx 10^{-8}$) about the reference initial condition $(\theta_0 \pm \epsilon, \phi_0 \pm \epsilon)$; then calculate the LLE from the reference solution and each of the other 16 solutions, and finally calculate an average. When $\langle\lambda\rangle$ is positive the system is chaotic, when $\langle\lambda\rangle$ is close to zero the system is periodic or quasiperiodic, and when $\langle\lambda\rangle$ is negative the system approaches a fixed point.

In Fig. 1, the components of $\boldsymbol{m}$ are plotted over the last 100 drive periods from 1238 to 1337 ns in an effort to understand the long-term behavior or final state of the system. When there is only one point for a given drive amplitude (or what appears to be a small spread) the magnetization is under period-one motion, and when there are two points the magnetization is under period-two motion, and so on. If there appears to be a continuum of points the motion may, in principle, be quasiperiodic or chaotic. When the bifurcation diagram reveals a transition from one type of behavior to another (i.e., period-one to quasiperiodic), the system underwent a bifurcation event near some critical value of the control parameter. The nature and classification of possible bifurcation events are well documented in nonlinear dynamics studies (see Refs. [44,45] for further investigation). Figure 1 reveals bifurcation events near 0.41, 1.38, and 2.45 kOe. Near each of these critical drive amplitudes the period-one motion becomes quasiperiodic, then transitions back to period-one motion oriented opposite the original m_3 direction (magnetization flip). As the drive amplitude is increased the oscillation amplitude increases and explores more of the unitary sphere, but on average $\boldsymbol{m}$ is oriented along the plus or minus z axis near the bifurcation events. We note that in the earlier studies [29] only the first transition was uncovered. Now, examining larger drive amplitudes, we see that an entire series of reversals are possible.

When the bifurcation events are accompanied by the LLE one can easily determine whether continuum regions in the bifurcation diagrams are chaotic or quasiperiodic. We see that $\langle\lambda\rangle \approx 0$ for the entire range of drive amplitudes shown in Fig. 1, and therefore, the continuum regions (bifurcation events) correspond to quasiperiodicity and not chaos. We believe that the slight deviations of $\langle\lambda\rangle$ away from zero before and after the bifurcation events are due to trajectories not being on the attractor. Prolonged quasiperiodic transient behavior is observed near each bifurcation event of the spherical system (as will be shown later), and increasing simulation times beyond 1337 ns for $\langle\lambda\rangle$ in Fig. 1 has shown further convergence of $\langle\lambda\rangle$ toward zero near the critical drive amplitudes. Therefore, the small deviations away from zero are due to trajectories that have yet to reach the attractor over the 1337 ns simulation time. In general as we extend the time for the calculation of $\langle\lambda\rangle$ its magnitude is reduced, indicating that this is numerical and not an indication of chaos, for example.

For the sphere and other geometric domains that we will examine in what follows, we have considered nearly 1 million initial conditions uniformly distributed over the unitary sphere [see Fig. 7(a), for example]. For any value of h_d, both the linearly and circularly driven spherical domains contain only one attracting limit cycle for each of the initial conditions investigated, and thus only one basin of attraction. In the spherical system, changes in the initial conditions only
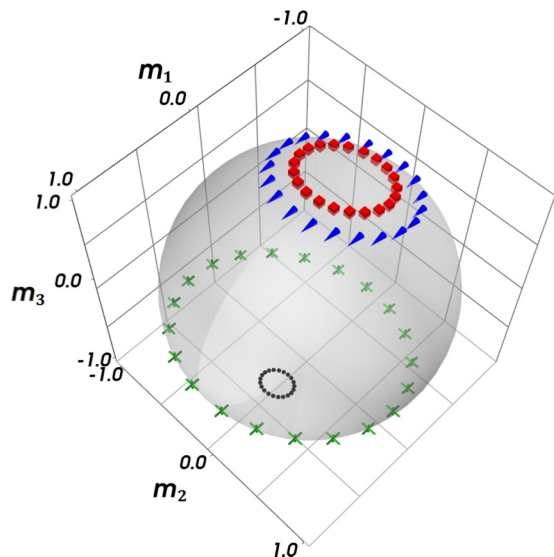
FIG. 2. Poincaré sections over different time intervals of the linearly polarized driven spherical domain at a critical drive amplitude of $h_d = 0.41$ kOe. Cubes: $t = 2475.2$–2495.2 ns; cones: $t = 24742.9$–24762.9 ns; asterisks: $t = 123711.5$–123731.5 ns; spheres (circles) $t = 247422.0$–247442.0 ns. $N_{11} = N_{22} = N_{33} = 1/3$, $\omega_d = 2\pi$ rad/ns, $\omega_0 = 1.84$ rad/ns, $h_s = 0.1$ kOe, $\alpha = 0.01$, and $(\theta_0 = 0, \phi_0 = 0)$.

resulted in differing times to reach the particular attractor. Therefore, while Fig. 1 only represents one initial condition $(\theta_0 = 0, \phi_0 = 0)$ its overall structure can qualitatively represent other initial conditions. The initial condition $(\theta_0 = 0, \phi_0 = 0)$ also represents an experimentally reasonable situation as the magnetization will be in line with the external static field $h_s \hat{z}$ before the microwave field is turned on. When the drive amplitude is zero for any of the magnetic geometries and the initial condition is $(\theta_0 = 0, \phi_0 = 0)$ the magnetization remains in line with the external static field. Once the oscillatory field is turned on, the system's dissipative processes compete with the energy introduced from the oscillatory field.

Once the driving field is turned on in the linearly polarized driven spherical system, a small amplitude limit cycle appears near the $+z$ axis and grows in amplitude as the drive amplitude is increased from 0.0 to 0.41 kOe (the first bifurcation event). In this system the transient behavior is quite interesting. Early in time, ϕ oscillates near the normal mode frequency $(\omega_0 = 1.84$ rad/ns), then transitions to oscillating at the driving frequency $(\omega_d = 2\pi$ rad/ns) as the system comes into equilibrium with the external driving field. As the drive amplitude is increased toward the critical value of 0.41 kOe, the transient lifetime increases and the normal mode frequency is shifted to lower frequencies and persists for a longer period of time. Near the critical value the motion appears to be quasiperiodic, but seems to approach some sort of attractor as the simulation times are increased by a few orders of magnitude. Figure 2 illustrates this prolonged quasiperiodic behavior using Poincaré sections over various time intervals. The longest simulation time in Fig. 2 is 247 442 ns, 185 times longer than the simulation time used for the bifurcation diagram of Fig. 1, and the trajectory has yet to converge to a
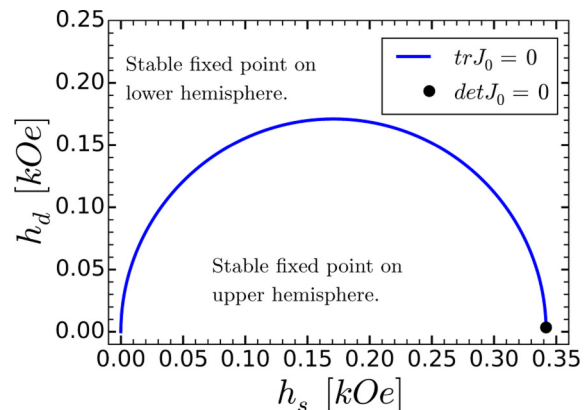

FIG. 3. Stability diagram for the circularly polarized driven spherical domain in the (h_d, h_s) plane. $N_{11} = N_{22} = N_{33} = 1/3$, $\omega_d = 2\pi$ rad/ns, and $\alpha = 0.01$.

particular attractor. At drive amplitudes greater than the critical value, the transient lifetime decreases and $\boldsymbol{m}$ finds an attractive limit cycle in the southern hemisphere.

The previous results were for a linearly polarized driving field, where the oscillating field was along the x direction. In fact, the mathematics becomes somewhat simpler if we look at a circularly polarized driving field, and we can gain greater insight into the prolonged transient and switching behavior in this limit. The LLG equation (1) can be transformed to autonomous form if one exploits the symmetry of the system driven by a circularly polarized field perpendicular to the static field. The vector field $d\boldsymbol{m}/dt$ transforms as

$$\left(\frac{d\boldsymbol{m}}{dt}\right)_{\text{lab}} = \left(\frac{d\boldsymbol{m}}{dt}\right)_{\text{rot}} + \omega_d \hat{z} \times \boldsymbol{m} \qquad (4)$$

when moving to the frame rotating at ω_d about the z axis. The LLG equation becomes

$$\left(\frac{d\boldsymbol{m}}{dt}\right)_{\text{rot}} - \alpha\left[\boldsymbol{m} \times \left(\frac{d\boldsymbol{m}}{dt}\right)_{\text{rot}}\right]$$
$$= -\boldsymbol{m} \times [\boldsymbol{h}_{\text{eff}} - \omega_d \hat{z} + \alpha\omega_d(\boldsymbol{m} \times \hat{z})], \qquad (5)$$

where $\boldsymbol{h}_{\text{eff}} = (h_d - N_{11}m_1)\hat{x} - N_{22}m_2\hat{y} + (h_s - N_{33}m_3)\hat{z}$. The transformation allows one to perform a Taylor series linearization about the fixed points of the system. The Jacobian (J_0) or stability matrix derived from the linearization is used to classify the types of fixed points [3,44]. In Fig. 3 we have plotted the determinant and trace of J_0 equated to zero for the control parameters h_d and h_s. For the entire control plane there are two types of fixed points. For values of h_d and h_s that lie inside the semicircle there is a spiral node (stable focus) on the surface of the unit sphere in the upper hemisphere and a spiral repeller (unstable focus) in the lower hemisphere. Values of h_d and h_s outside the semicircle result in a spiral repeller on the upper hemisphere and a spiral node on the lower. The bifurcation diagram associated with a vertical line $h_s = 0.1$ kOe (Fig. 3) is shown in Fig. 4. Indeed, we see as the h_d crosses the $\text{tr}J_0 = 0$ line a bifurcation event occurs and the m_3 component of the magnetization switches from the upper to lower hemisphere. This magnetization switch occurs near $h_d = 0.15$ kOe, a value lower than that of the linearly driven system.
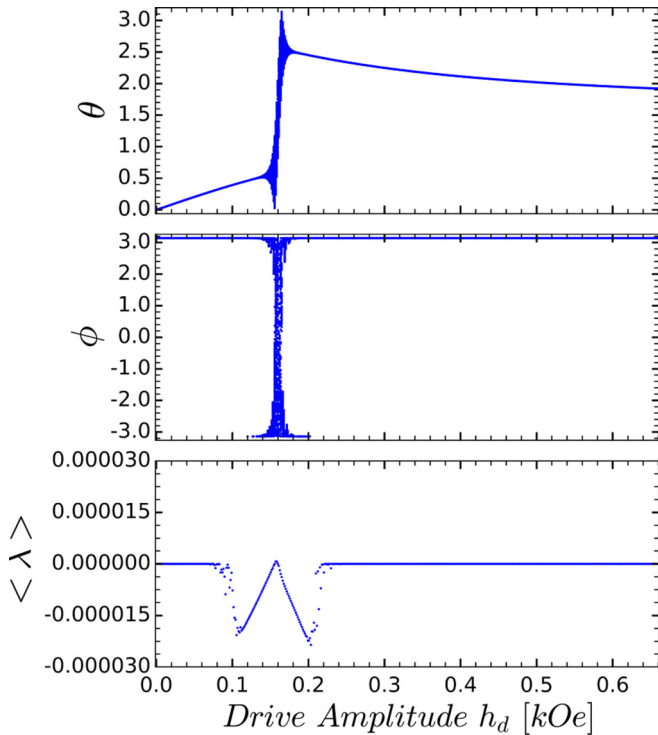
FIG. 4. Bifurcation diagram of the circularly polarized driven spherical domain and the average largest Lyapunov exponent $\langle\lambda\rangle$ as a function of h_d from 1238 to 1337 ns. $N_{11} = N_{22} = N_{33} = 1/3$, $\omega_d = 2\pi$ rad/ns, $\omega_0 = 1.84$ rad/ns, $h_s = 0.1$ kOe, $\alpha = 0.01$, and $(\theta_0 = 0, \phi_0 = 0)$.
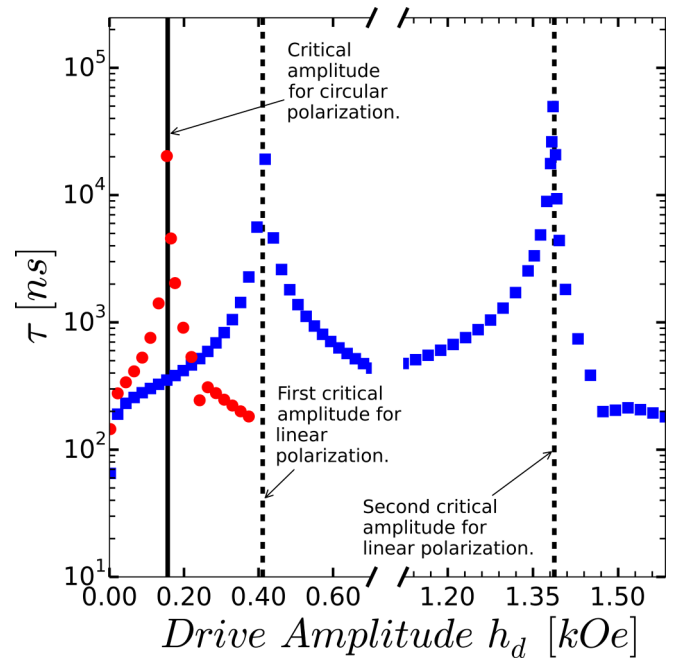

FIG. 5. Asymptotic behavior of transient lifetime as a function of drive amplitude for both the circularly and linearly polarized driven spherical domains. Circularly polarized: Circles asymptotically approaching the solid line. Linearly polarized: Squares asymptotically approaching the dashed line. $N_{11} = N_{22} = N_{33} = 1/3$, $\omega_d = 2\pi$ rad/ns, $\omega_0 = 1.84$ rad/ns, $h_s = 0.1$ kOe, $\alpha = 0.01$, and $(\theta_0 = 0, \phi_0 = 0)$.

Additional insights into the transient lifetime as h_d approaches the $\text{tr}J_0 = 0$ line in Fig. 3 can be made by considering the behavior of a small perturbation $\delta\boldsymbol{m}$ perpendicular to the fixed point $\boldsymbol{m}_0$. Qualitatively, the behavior can be described by

$$\delta m_{e1}(t) \sim e^{\chi t}\sin(\psi t), \quad \delta m_{e2}(t) \sim e^{\chi t}\cos(\psi t),$$

$$\chi = \tfrac{1}{2}\text{tr}J_0, \quad \psi = \tfrac{1}{2}\sqrt{|(\text{tr}J_0)^2 - 4\det J_0|}, \qquad (6)$$

where the subscripts $e1$ and $e2$ correspond to the plane tangent to the fixed point $\boldsymbol{m}_0$. Equation (6) tells us that δm_{e1} and δm_{e2} oscillate in time with frequency ψ, and the amplitude of the oscillations either increases or decreases exponentially depending on the sign of χ. For $\chi < 0$, Eq. (6) describes a spiraling trajectory converging on the fixed point and when $\chi > 0$, Eq. (6) describes a spiraling trajectory diverging from the fixed point. As $\chi \to 0^-$ the spiral trajectory takes more and more time to reach the fixed point. Similarly, as $\chi \to 0^+$ the spiral trajectory takes longer to diverge from the fixed point. Therefore, we should expect to find prolonged transients near the fixed points of this dynamic system as $\chi \to 0$ or equivalently as $\text{tr}J_0 \to 0$, and this is precisely what we have observed.

As highlighted above, the circularly polarized driven spherical system is similar in many ways to the linearly polarized system. Once the circularly polarized field is turned on (in the laboratory frame) the magnetization approaches a perfectly circular limit cycle in the upper hemisphere due to symmetry. In the frame rotating with the oscillatory field this limit cycle reduces to a fixed point. As the drive amplitude

is increased toward the bifurcation (Fig. 4) the attracting limit cycle becomes larger and the transient lifetime increases dramatically. Near the critical value $h_d = 0.15$ kOe the motion is quasiperiodic just as in the linearly driven system. At values greater than the critical field the magnetization switches to the lower hemisphere and the transient lifetime decays just as in the linearly polarized driven system. One interesting difference between the linearly polarized driving results and those found here for the circular polarization is that there are multiple reversals for the linear polarization and only one for the circular.

In Fig. 5, we highlight the asymptotic behavior of the transient lifetime τ in both the circularly and linearly polarized spherical systems. In our analysis we have defined τ as the amount of time it takes for consecutive Poincaré sections to differ by less than 0.001. In Fig. 5, the circles asymptotically approaching the solid line represent the circularly polarized case, while the squares asymptotically approaching the dashed line correspond to the linearly polarized case. At the drive amplitudes given by the vertical lines, the simulations did not settle into an attractor. Therefore, all we can say is that τ must be greater than 247 442 ns (our longest simulation time) at these drive amplitudes.

Modification of the demagnetization factors by a few percent (2%–3%) from perfect spherical symmetry show similar behavior for both circularly and linearly driven systems. Changes in the demagnetization factors larger than a few percent can lead to complex limit cycles of multiple periods and chaos. In the linearly driven system, increasing

the frequency ratio ω_d/ω_0 pushes the bifurcation events to larger values h_d, while simultaneously spreading how often they occur along the h_d axis. Decreasing ω_d/ω_0 to values near 1, leads to opposing behavior; the bifurcation events occur at lower values of h_d and occur at a greater frequency along the h_d axis. Of course, if we move to frequency ratios too large or too small these discussion points may not hold. For example, decreasing ω_d/ω_0 to really low values, such as 0.05 in the linearly driven system, produces very minor coupling to the system and the system will take an extremely long time to come into equilibrium with the fields. Increasing ω_d/ω_0 in the circularly driven system moves the one bifurcation event to larger values of h_d, while decreasing ω_d/ω_0 drives the bifurcation to lower values of h_d, until $\omega_d/\omega_0 < 1$. For $\omega_d/\omega_0 < 1$, in the circularly driven system, no bifurcation events were observed, and with increasing h_d the system finds its equilibrium in a circular orbit on the equator.

We comment on the possibility to observe these dynamic magnetization reversals experimentally. All the methods would involve placing spherical nanoparticles in ultrasmall waveguides, for example, in a narrow gap between the signal line and the ground planes in a coplanar waveguide. This would generate the large oscillating fields required for these measurements. The average z component of the magnetization of a collection of nanoparticles could then be probed optically through a magneto-optic Kerr effect measurement, for example [46]. A second possibility is to use a variation of a pulsed inductive magnetic magnetometer [47] which uses a fast oscilloscope (20 GHz) to measure the actual time-dependent dynamics. Finally, it is likely that the permeability at a given frequency would show significant changes at the critical amplitudes that produce magnetic reversals. This could be measured directly as a change in the reflected (S_{11}) or transmitted (S_{21}) signal propagating down the waveguide using a network analyzer [48].

IV. LONG CYLINDRICAL DOMAIN

The strong dynamic demagnetization field associated with a long cylindrical domain ($N_{11} = N_{22} = 1/2$, $N_{33} = 0$) results in the magnetization coming to equilibrium with the external driving field in a much shorter time interval than the sphere. In addition, interesting bifurcation events did not occur until the drive amplitude was well over 1000 Oe. We note that the use of finite cylinders gives similar results, but the key amplitudes for h_d are all much lower. For example, with the parameters $N_{11} = N_{22} = 0.4$, $N_{33} = 0.2$ the important driving amplitudes all drop by about an order of magnitude. (Of course, the important frequencies for the driving field need to be reduced in this case because the resonance frequency is lowered significantly.) The normal mode frequency associated with the long cylinder is $\omega_0 = 203.9$ rad/ns with $h_s = 0.1$ kOe, two orders of magnitude larger than the sphere, and therefore we apply a higher frequency oscillatory field at $\omega_d = 686.3$ rad/ns. Here, the frequency ratio (ω_d/ω_0) does not exactly equal 3.4, but is quite close at $\omega_d/\omega_0 = 3.37$. These slight differences are due to how we have implemented our Poincaré sections and bifurcation algorithms. The code we developed requires the drive period to be exactly divisible by the step size. This
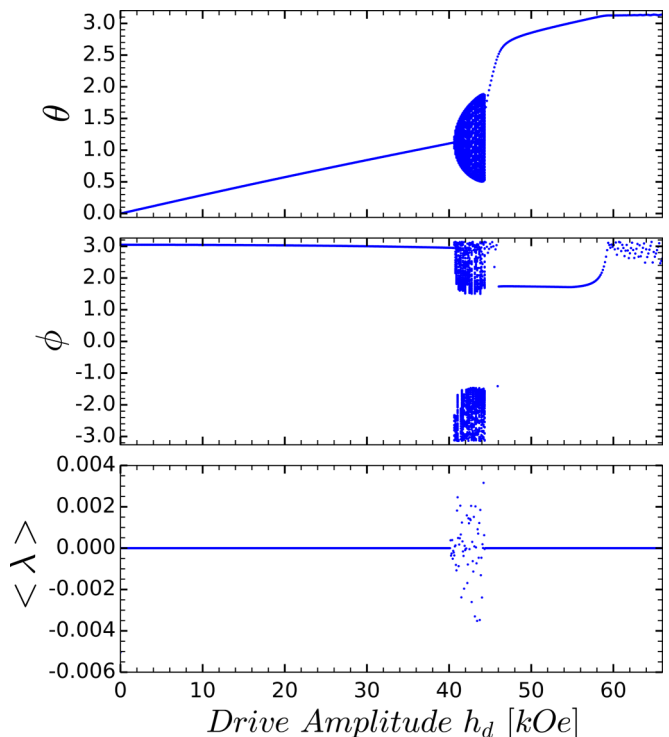

FIG. 6. Bifurcation diagram of the linearly polarized driven cylindrical domain and the average largest Lyapunov exponent $\langle \lambda \rangle$ as a function of h_d from 1238 to 1337 ns. $N_{11} = N_{22} = 1/2$, $\omega_d = 686.3$ rad/ns, $\omega_0 = 203.9$ rad/ns, $h_s = 0.1$ kOe, $\alpha = 0.01$, and ($\theta_0 = 0, \phi_0 = 0$).

ensures that the Poincaré sections taken every drive period fall precisely on a data point and we do not have to interpolate.

The initial state (i.e., initial condition) of the cylindrical system is more important here than the spherical system, due to the demagnetization field directing ***m*** along the axis of symmetry (the z axis). In the low field limit ($h_d \lesssim 0.1$ kOe) in both linearly and circularly driven systems, and with the initial state anywhere on the upper hemisphere, the trajectory always finds an attractive limit cycle near the $+z$ axis. Similarly, if the initial state is on the lower hemisphere, the trajectory finds a limit cycle near the $-z$ axis. As h_d is increased the division outlined above between the upper and lower hemispheres becomes skewed. The bifurcation diagram and average LLE of the linearly driven system is shown in Fig. 6 for an initial state on the upper hemisphere ($\theta_0 = 0$, $\phi_0 = 0$). In contrast to the sphere where the largest value of $\langle \lambda \rangle$ was on the order of $\pm 10^{-5}$ throughout the range of drive amplitudes simulated, here in Fig. 6, we see $\langle \lambda \rangle$ on the order of $\pm 10^{-3}$ in the range $40 \lesssim h_d \lesssim 45$ kOe. This suggests a stronger sensitivity to the initial conditions over the range $40 \lesssim h_d \lesssim 45$ kOe, but $\langle \lambda \rangle$ is still small compared to other LLE values where stronger chaotic behaviors are observed (see $\langle \lambda \rangle$ in Fig. 9, for example), and when viewing the detailed oscillatory information in this band the motion appears to be quasiperiodic. Therefore, the band over the range $40 \lesssim h_d \lesssim 45$ kOe corresponds to quasiperiodic behavior with more sensitivity to initial conditions than seen for drive amplitudes less than 40 kOe and greater than 45 kOe.
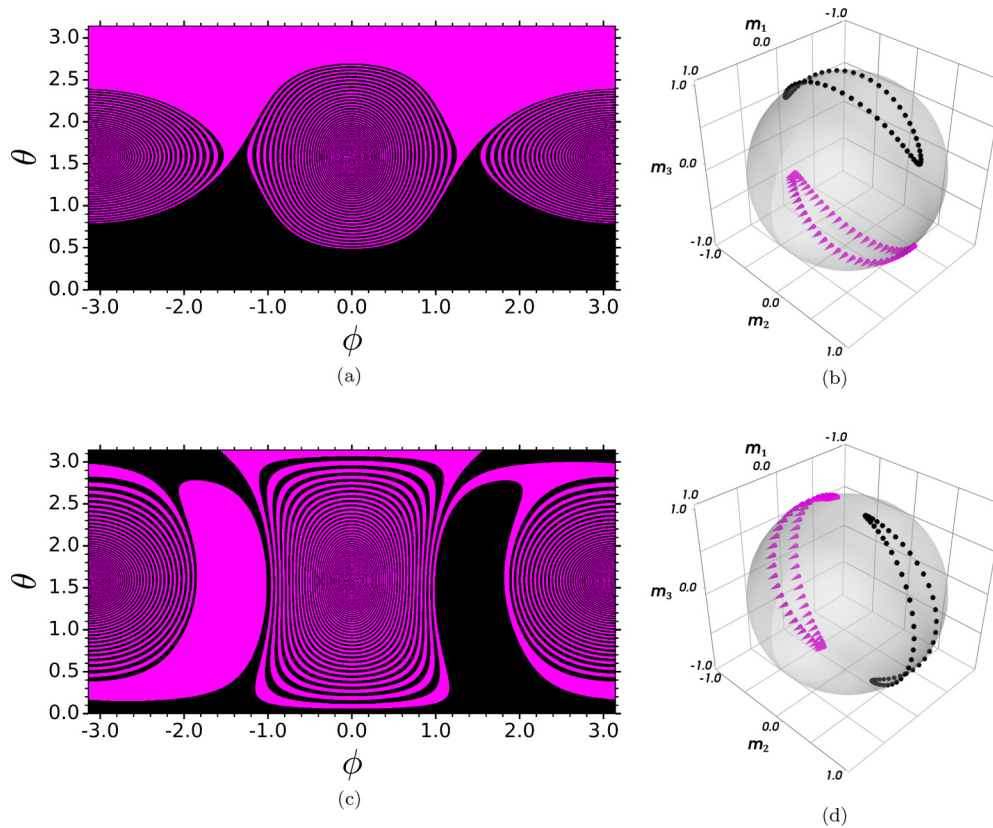
(a)

(b)

(c)

(d)

FIG. 7. Basins of attraction and corresponding attractors for the linearly polarized driven cylindrical domain with different values of the drive amplitude. (a) and (c) are the basins of attraction for the attractors shown in (b) and (d), respectively. (a) $h_d = 38.04$ kOe; (b) $h_d = 38.04$ kOe; (c) $h_d = 47.94$ kOe; and (d) $h_d = 47.94$ kOe.

The bifurcation diagram for an initial state in the lower hemisphere looks qualitatively similar to that shown in Fig. 6. For example, when $(\theta_0 = \pi, \phi_0 = 0)$ θ starts at π and undergoes similar period-one motion on the lower hemisphere until the first bifurcation event near 40 kOe; then undergoes similar quasiperiodic behavior (but now in the lower hemisphere) over the range $40 \lesssim h_d \lesssim 45$ kOe; and finally, for $h_d \gtrsim 45$ kOe, has similar period-one behavior.

In Fig. 7, we present the basins of attraction in (a) and (c) and corresponding attractors in (b) and (d) of the linearly polarized driven cylindrical system for drive amplitudes before and after the quasiperiodic region. (A basin of attraction is the set of initial conditions that leads to a particular attractor.) Unlike the sphere (where different initial states lead to the same attractor), this system is a two-state system throughout the range of drive amplitudes investigated (0–66 kOe). This is primarily due to the constraint of the demagnetization field along the axis of symmetry. Figure 7(a) reveals two interlocking spiral basins of attraction near the equator. As highlighted earlier, in the low field limit the basins are divided along the equator, and with increasing h_d, the basins start to explore a larger region about the equator of the unitary sphere. In Fig. 7(a), at $h_d = 38.04$ kOe, the division between the upper and lower hemispheres is still apparent, but near the equator the system may evolve toward either attractor. In Fig. 8 we have plotted a subsection of Fig. 7(a) using nearly 1 million initial conditions. Within the quasiperiodic region ($40 \lesssim h_d \lesssim 45$ kOe) the system finds different quasiperiodic attractors oriented about

the $+z$ or $-z$ poles, depending on the initial state. After the quasiperiodic region ($h_d \gtrsim 45$ kOe), Fig. 7(c) reveals similar interlocking spiral basins of attraction, but now the attractors are oriented along the $\pm y$ (m_2) directions.
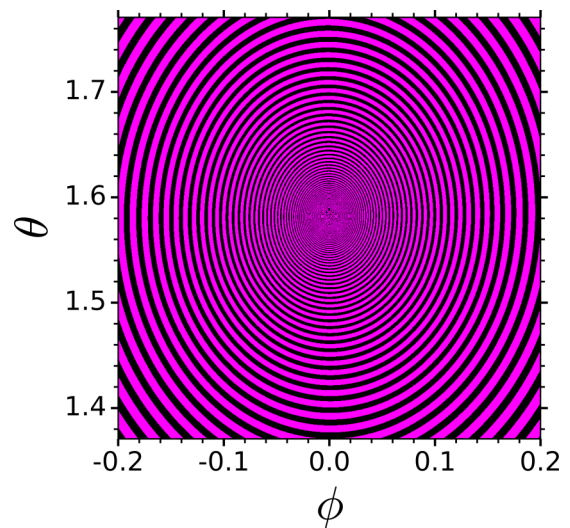

FIG. 8. Subsection of Fig. 7(a). Basins of attraction using nearly 1 million initial conditions for the linearly polarized driven cylindrical domain when $h_d = 38.04$ kOe.

Note that the spacing between points on the three dimensional (3D) attractor plots in Figs. 7(b) and 7(d), are for illustration purposes only (to show the location of the final state of the system). In reality, they represent continuous magnetization curves within those regions of the unit sphere. Similar 3D attractor plots with various point spacings are shown later in Figs. 10(b), 10(d), and 10(f), and those are meant to represent continuous magnetization curves as well.

When the long cylinder is driven by a circularly polarized field the dynamics are again simplified greatly due to the autonomous nature of the LLG equation in this system. In addition, the rotational symmetry and uniform magnetization prevents the emergence of a chaotic state [3]. Two-dimensional state space systems cannot have chaotic trajectories as a result of the Poincaré-Bendixson theorem [44]. Under a low driving field, the circularly polarized system approaches one of two attractors on the upper or lower hemisphere, depending on whether the initial state starts in the upper or lower hemisphere (just as in the linearly polarized case). Unlike the elongated limit cycles of the linearly polarized cylindrical domain [see Fig. 7(b), for example], the attracting limit cycles are perfect circles due to the symmetry of the circularly polarized system. As the drive amplitude is increased the amplitude of the limit cycles becomes larger and the basin of attraction of the upper hemisphere begins to erode. Only one bifurcation event was observed for this system at $h_d \approx 15$ kOe. This bifurcation coincided with the complete erosion of the upper hemisphere's basin of attraction, thereby creating a one-state system that only evolves toward a single attractor in the lower hemisphere (no matter where the initial state began). The determinant and trace of the stability matrix of this system do not predict where the bifurcation events occur as was found in the spherical system. The reason for this is that one needs to study the stability of limit cycles instead of the stability of fixed points. A stability analysis of this system can be developed by analyzing the zeros of the Melnikov function, where one investigates the stability of limit cycles [2,3,16,18].

Similar to the spherical system, increasing the ratio ω_d/ω_0 results in the bifurcation events occurring at larger values of h_d in both the linearly and circularly driven systems. Decreasing ω_d/ω_0 to values near 1, moves bifurcations to lower values of h_d. In the linearly driven system, decreasing ω_d/ω_0 shifts the quasiperiodic region shown in Fig. 6 to lower values of h_d, and as ω_d/ω_0 approaches 1, this quasiperiodic region seems to transform into a chaotic region.

V. INFINITE PLANE (THIN-FILM) DOMAIN

The magnetic thin-film geometry is probably the most commonly studied. Of course, to have a single domain one needs to have a small structure, with lateral dimensions on the order of 50 nm or less so that domain walls are too costly to form. In this section we use the demagnetizing factors of an infinite plane ($N_{11} = 0$, $N_{22} = 1$, $N_{33} = 0$). One can get close to these values for films with a thickness on the order of just a few nanometers with the lateral dimensions quoted above. For example, using the analytic expression for the demagnetization factors developed by Aharoni [49], a square geometry with the
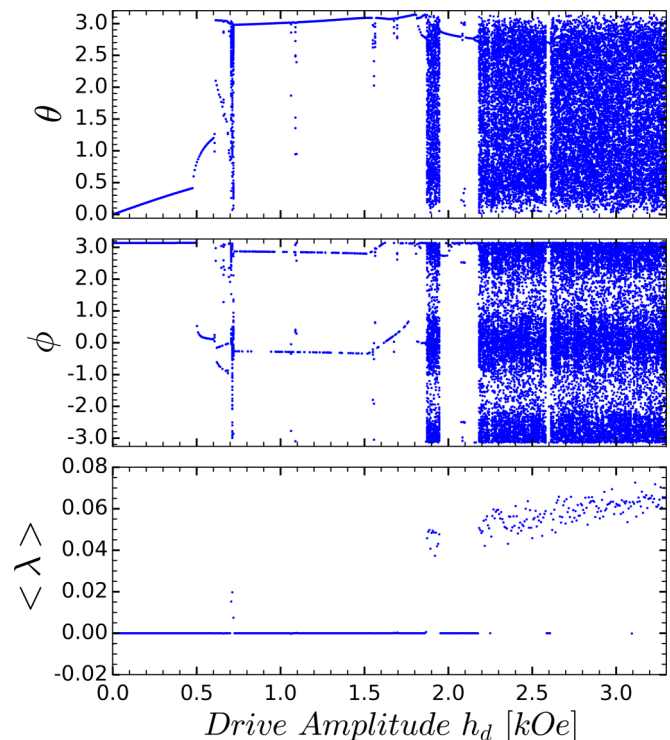

FIG. 9. Bifurcation diagram of the linearly polarized driven thin-film domain and the average largest Lyapunov exponent $\langle \lambda \rangle$ as a function of h_d from 1238 to 1337 ns. $N_{22} = 1$, $\omega_d = 93.4$ rad/ns, $\omega_0 = 27.3$ rad/ns, $h_s = 0.1$ kOe, $\alpha = 0.01$, and ($\theta_0 = 0, \phi_0 = 0$).

50 nm side length and a thickness of 2 nm has $N_{11} = 0.05$, $N_{22} = 0.9$, $N_{33} = 0.05$.

As with the long cylindrical domain, the thin-film systems we have investigated came into equilibrium with the external driving field in a shorter time interval than that of the spherical domain due to the strong dynamic demagnetization field of the thin-film geometry. The choice of $N_{22} = 1$ breaks the rotational symmetry of the circularly driven system and allows the dynamics for both the linearly and circularly polarized driving fields to eventually become chaotic in certain regions of the phase space. This is in contrast to the results for the circularly polarized case in the cylinder and sphere where the solution is never chaotic.

The bifurcation diagrams of both the linearly and circularly polarized driving fields show similar behavior as a function of drive amplitudes, and therefore we only show the linearly polarized case in Fig. 9. Under low drive amplitudes this is expected because the strong demagnetizing field overwhelms the y component of the circularly driven field. The natural frequency for this system is 27.3 rad/ns and for our example results, we pick a driving frequency that is about a factor of 3.4 larger than this. Figure 9 was derived using a single initial condition ($\theta_0 = 0, \phi_0 = 0$), just as was the case for the sphere and cylinder systems, and just like those systems, the thin-film bifurcation diagrams using other initial conditions produces qualitatively similar results. In other words, the period-one, period-two, etc., and chaotic regions for other initial conditions appear over similar drive amplitude intervals as that shown in Fig. 9.
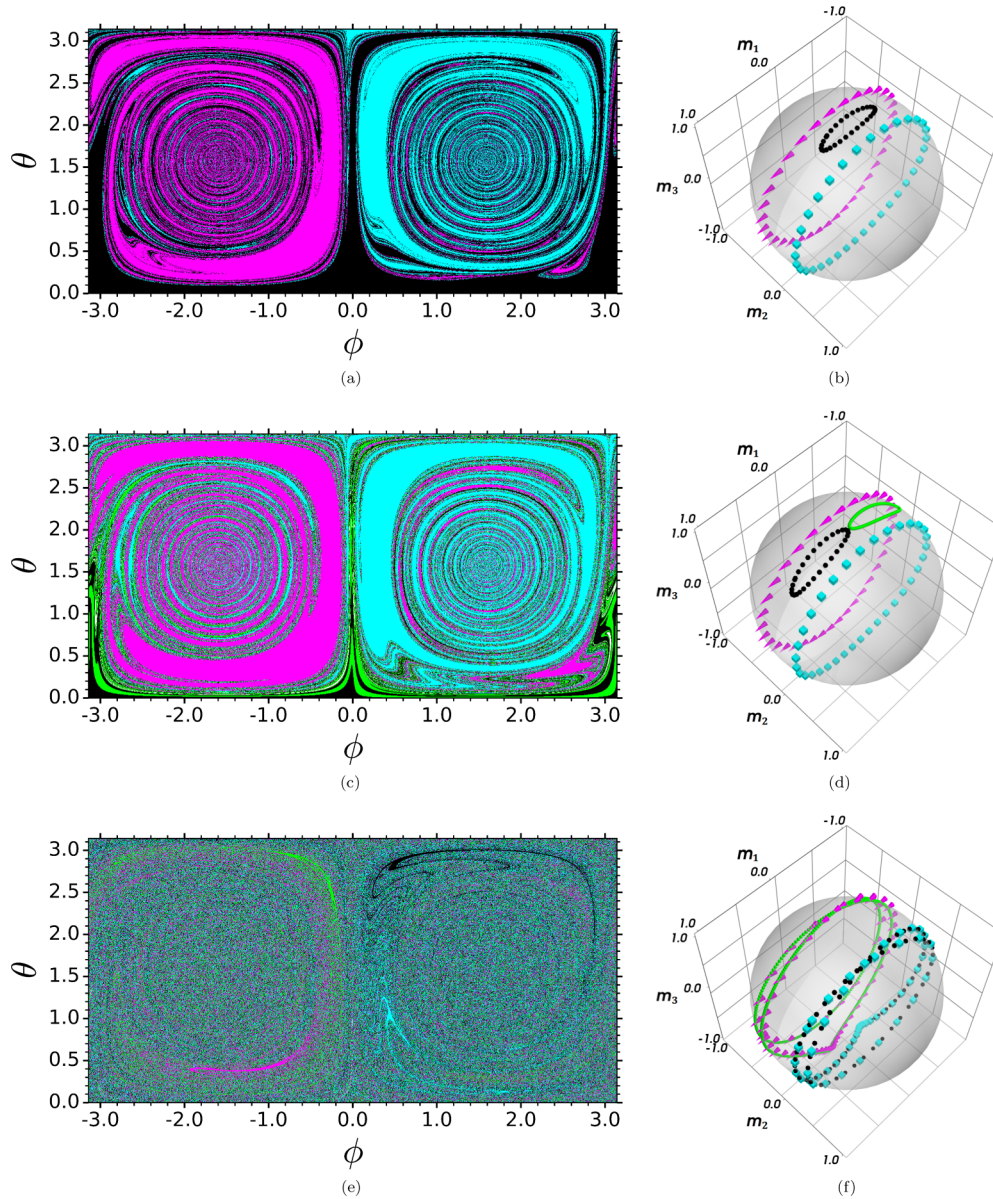
FIG. 10. Basins of attraction and corresponding attractors for the linearly polarized driven thin-film domain with different values of the drive amplitude. (a), (c), and (e) are the basins of attraction for the attractors shown in (b), (d), and (f), respectively. (a) $h_d = 0.40$ kOe; (b) $h_d = 0.40$ kOe; (c) $h_d = 0.50$ kOe; (d) $h_d = 0.50$ kOe; (e) $h_d = 0.67$ kOe; and (f) $h_d = 0.67$ kOe.

In the low field ($h_d \lesssim 0.1$ kOe) limit for both of the driven thin-film systems there is only one low amplitude attracting limit cycle near the $+z$ pole, which oscillates at the drive frequency $\omega_d = 93.4$ rad/ns. Near $h_d = 0.1$ kOe both systems developed two additional small basins of attraction. These two new attractors exhibit large amplitude motion in the (m_1, m_3) plane and their basins of attraction grow in area and become riddled with increasing h_d. Figures 10(a) and 10(b) show the riddled basins of attraction and corresponding attractors when $h_d = 0.40$ kOe in the linearly driven system (just before the first bifurcation event). Even though the basins are complicated, one can readily see that if we choose to divide the upper and lower hemispheres by the plane $y = 0$ instead of $z = 0$, the probability of an initial state in the upper hemisphere finding the attractor in the lower hemisphere is lower than finding the one near its original state. With a sufficiently

dense initial condition grid, one could easily quantify the probabilities any random selection would yield a particular attractor. For example, using the 980 000 solutions used to plot Fig. 10(a), the fractions of each attractor are black: $\sim$0.45; magenta: $\sim$0.28; cyan: $\sim$0.27.

The first bifurcation event (near $h_d = 0.49$ kOe) in the linearly driven system corresponds with the simultaneous creation of an additional small amplitude attracting limit cycle near the $+z$ pole [see Figs. 10(c) and 10(d)] and a period-five attractor that can have different phases depending on its basin. The period-five attractors are represented by the white basin that reveals itself when we zoom in on a subsection of Fig. 10(c). Figure 11 is a zoomed-in plot of a small section of Fig. 10(c) that clearly shows five different basins. The period-five attractors are not shown in Fig. 10(d) for clarity of the other attractors. The period-five attractor would lay atop the
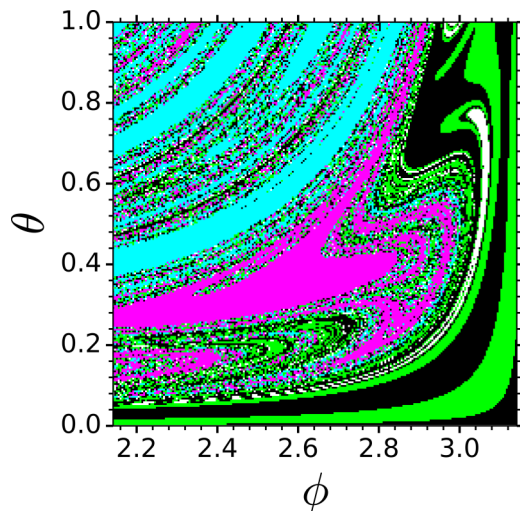
FIG. 11. Zoomed-in view of a small section of Fig. 10(c) that reveals five different riddled basins of attraction. The white basin corresponds to period-five attractors of various phases, and the remaining basins correspond to the attractors shown in Fig. 10(d).

two smaller attractors near the $+z$ pole and appear as a complex limit cycle with various lobes. Similar behavior is observed near the first bifurcation of the circularly driven system, but we did not observe any period-five attractors using the same initial condition grid. Maybe the period-five basins are much smaller in the circularly driven system or they may not develop due to the differing dynamics. One possibility for the differences is that Fig. 9 shows a small region exhibiting chaotic behavior near $h_d = 0.7$ kOe; this small chaotic region does not appear in the circularly driven system. (The circularly driven system does show chaotic behavior, but only when values of h_d are $\gtrsim 1.6$ kOe.) Therefore, the creation of the period-five attractors of differing phases in the linear system may be linked to that system's route to chaos near $h_d = 0.7$ kOe, although further investigation is required.

Increasing h_d from ~ 0.5 to ~ 0.6 kOe in the linearly driven system results in the two small amplitude limit cycles in Fig. 10(d) diverging from one another (the large amplitude attractors remain relatively stationary). Near 0.6 kOe another bifurcation occurs and gives rise to multiperiodic attractors and highly irregular basins until the chaotic region near 0.7 kOe. Figures 10(e) and 10(f) show this behavior at $h_d = 0.67$ kOe. Figure 10(f) shows four period-two attractors, where the black spheres are intermingled with the cyan cubes and lie atop one another, and the magenta cones are intermingled with the lime line. These attractors have strong harmonics at $0.5\omega_d$ and $1.5\omega_d$, and lie atop one another, but are phase shifted from each other when one views the detailed oscillatory information. The white basin in Fig. 10(e) is only visible when one zooms in to the high-resolution image, and it corresponds to two small amplitude period-five attractors not shown, but which lie between (sandwiched) the four period-two attractors in Fig. 10(f). Therefore, the destruction of the two small amplitude period-one limit cycles in Fig. 10(d) leads to large amplitude multiperiodic motion, and finally, chaos near 0.7 kOe. Surprisingly, just after the first chaotic region ($\gtrsim 0.7$ kOe), the linearly driven system turned into a

two-state system for most of the drive amplitudes from ~ 0.7 to ~ 1.85 kOe, with only two basins of attraction and two period-one attractors that look very similar to the large amplitude (in the m_1 and m_3 plane) attractors in Fig. 10(b). Even though the attractors are much simpler than that described leading up to 0.7 kOe, the two basins of attraction are highly irregular with no discernible pattern. From ~ 0.7 to ~ 1.85 kOe the two period-one attractors become warped and near 1.85 kOe collide with one another and the system reverts back into chaos. The regions near h_d of 1.08, 1.55, and 1.68 kOe (Fig. 9) are brief excursions into multiperiodic behavior from the two-state period-one behavior described above. Periodic motion is again briefly restored over the range $1.95 \lesssim h_d \lesssim 2.18$, and then predominantly chaotic for the rest of the drive amplitudes simulated. Similar behaviors are observed when driven by the circularly polarized field, but the transitions from one kind of behavior to another occur at slightly different values of the drive amplitude h_d than that described above.

Just as in the sphere and cylinder systems, increasing ω_d/ω_0 leads to bifurcations occurring at greater values of h_d, while decreasing ω_d/ω_0 to values near 1 results in chaotic behavior and bifurcations occurring at lower values of h_d.

VI. CONCLUSIONS

We have explored the dynamic behavior of the magnetization in a variety of nanoparticles when driven by large amplitude oscillating fields. To characterize this, we studied bifurcation diagrams, Lyapunov exponents, chaos, and basins of attraction for three different characteristic geometries: spheres, cylinders, and planes. For the sphere we examined systems driven with both linear and circularly polarized driving fields. We observed only one attracting limit cycle for a large number of initial conditions and quasiperiodic prolonged transient behavior near the bifurcation events. These bifurcations resulted in a magnetization flip of the m_3 component. The autonomous form of the circularly driven spherical system allowed us to predict where the prolonged transient behavior will occur as a function of the external field control parameters. The stability analysis also allowed us to qualitatively describe why the transient lifetime increased as one approached the $\mathrm{tr} J_0 = 0$ in Fig. 3. Variations in the demagnetization factors greater than a few percent in the sphere can lead to more than one attractor, multiperiodic orbits, and chaos.

In the low field limit ($h_d \lesssim 0.1$ kOe) of the linearly polarized driven cylindrical system the two basins of attraction are divided along the equator. When $\boldsymbol{m}$ starts in the upper hemisphere it will find the attractor in the upper hemisphere, and when $\boldsymbol{m}$ starts in the lower hemisphere it will find the attractor in the lower hemisphere. Increasing the drive amplitude skews the division between the basins in the upper and lower hemispheres until the first bifurcation. The first bifurcation results in period-one attractors in the upper and lower hemisphere becoming quasiperiodic. Further increasing h_d resulted in the quasiperiodicity disappearing and the system reorienting itself along the y axis. Chaos was not observed for this system for the parameters presented, but chaos was observed when reducing the frequency ratio ω_d/ω_0 to 1.4.

The circularly driven cylindrical system showed a similar division between basins of attraction on both the upper and lower hemispheres in the low field limit ($h_d \lesssim 0.1$ kOe). Increasing h_d in this system led to the erosion of the upper basin. The only bifurcation event observed for this system occurred simultaneously with the complete erosion of the upper basin of attraction.

The linearly and circularly driven thin-film domains showed similar behaviors throughout the range of drive amplitudes investigated. These systems go through many transitions over the range of drive amplitudes investigated. In the low field limit ($h_d \lesssim 0.1$ kOe) there is only one attractor for either system. Near $h_d = 0.1$ kOe both systems developed two additional small basins of attraction which corresponded to large amplitude motion in the (m_1, m_3) plane. As the drive amplitude increased further, the basins grew in area and developed a riddled structure. The first bifurcation event in either system coincided with the appearance of an additional small amplitude limit cycle near the $+z$ pole. Further increasing h_d resulted in the two small amplitude period-one attractors diverging from one another until the next bifurcation event, which resulted

in the creation of large amplitude multiperiodic attractors. Further increasing h_d led to a brief chaotic region in the linearly driven system, after which, the system became a two-state system. The circularly driven system did not have the brief transition to chaos, but nonetheless transitioned to a twostate system just as did the linearly driven system. The linearly driven system is primarily chaotic when $h_d \gtrsim 2.18$, and the circularly driven system is primarily chaotic when $h_d \gtrsim 1.6$ kOe.

The LLG equation, along with its many adjustable parameters provides a rich amount of nonlinear and chaotic phenomena in magnetic systems. We have surveyed the dynamic behavior of the magnetization near bifurcation events for different monodomain shapes where an external linearly or circularly polarized oscillating field is perpendicular to an external static field. The particular orientation of the external fields was chosen to be representative of common experimental setups, such as those used in ferromagnetic resonance experiments. The extensive survey presented in this paper provides a foundation for investigations into other LLG systems with additional complexities.

[1] T. L. Gilbert, IEEE Trans. Magn. **40**, 3443 (2004).

[2] C. Serpico, I. Mayergoyz, G. Bertotti, M. d'Aquino, and R. Bonin, Phys. B (Amsterdam, Neth.) **403**, 282 (2008).

[3] I. D. Mayergoyz, G. Bertotti, and C. Serpico, *Nonlinear Magnetization Dynamics in Nanosystems* (Elsevier, New York, 2009).

[4] D. Wei, *Micromagnetics and Recording Materials* (Springer Science and Business Media, Heidelberg, 2012).

[5] M. d'Aquino, W. Scholz, T. Schrefl, C. Serpico, and J. Fidler, J. Magn. Magn. Mater. **290**, 510 (2005).

[6] P. E. Wigen, *Nonlinear Phenomena and Chaos in Magnetic Materials* (World Scientific, Singapore, 1994).

[7] K. Takano, X. Zhang, E.-A. Salhi, L. Guan, M. Sakai, J. Smyth, and M. Dovek, IEEE Trans. Magn. **43**, 2184 (2007).

[8] H. Forster, T. Schrefl, W. Scholz, D. Suess, V. Tsiantos, and J. Fidler, J. Magn. Magn. Mater. **249**, 181 (2002).

[9] M. Getzlaff, *Fundamentals of Magnetism* (Springer Science and Business Media, Berlin, 2007).

[10] J. Osborn, Phys. Rev. **67**, 351 (1945).

[11] G. Bertotti, C. Serpico, I. Mayergoyz, R. Bonin, and M. d'Aquino, J. Magn. Magn. Mater. **316**, 285 (2007).

[12] J. Bragard, H. Pleiner, O. J. Suarez, P. Vargas, J. A. C. Gallas, and D. Laroze, Phys. Rev. E **84**, 037202 (2011).

[13] M. d'Aquino, S. Perna, C. Serpico, G. Bertotti, I. Mayergoyz, and A. Quercia, Phys. B (Amsterdam, Neth.) **486**, 126 (2016).

[14] M. d'Aquino, A. Quercia, C. Serpico, G. Bertotti, I. Mayergoyz, S. Perna, and P. Ansalone, Phys. B (Amsterdam, Neth.) **486**, 121 (2016).

[15] S. I. Denisov, T. V. Lyutyy, B. O. Pedchenko, and O. M. Hryshko, Phys. Rev. B **94**, 024406 (2016).

[16] D. Laroze, D. Becerra-Alonso, J. A. Gallas, and H. Pleiner, IEEE Trans. Magn. **48**, 3567 (2012).

[17] R. Sarmah and G. Ananthakrishna, Commun. Nonlin. Sci. Num. Simul. **19**, 3880 (2014).

[18] C. Serpico, J. Magn. Magn. Mater. **290**, 48 (2005).

[19] L. F. Alvarez, O. Pla, and O. Chubykalo, Phys. Rev. B **61**, 11613 (2000).

[20] C. Tannous and J. Gieraltowski, Eur. J. Phys. **29**, 475 (2008).

[21] D. Laroze, J. Bragard, O. J. Suarez, and H. Pleiner, IEEE Trans. Magn. **47**, 3032 (2011).

[22] T. V. Lyutyy, S. I. Denisov, A. Y. Peletskyi, and C. Binns, Phys. Rev. B **91**, 054425 (2015).

[23] J. Rácz, P. F. de Châtel, I. A. Szabó, L. Szunyogh, and I. Nándori, Phys. Rev. E **93**, 012607 (2016).

[24] Y. Khivintsev, J. Marsh, V. Zagorodnii, I. Harward, J. Lovejoy, P. Krivosik, R. Camley, and Z. Celinski, Appl. Phys. Lett. **98**, 042505 (2011).

[25] Y. Khivintsev, B. Kuanr, T. J. Fal, M. Haftel, R. E. Camley, Z. Celinski, and D. L. Mills, Phys. Rev. B **81**, 054436 (2010).

[26] J. Marsh, V. Zagorodnii, Z. Celinski, and R. Camley, Appl. Phys. Lett. **100**, 102404 (2012).

[27] C. Cheng and W. E. Bailey, Appl. Phys. Lett. **103**, 242402 (2013).

[28] G. Woltersdorf and C. H. Back, Phys. Rev. Lett. **99**, 227207 (2007).

[29] M. Phelps, K. Livesey, A. Ferona, and R. Camley, Europhys. Lett. **109**, 37007 (2015).

[30] R. K. Smith, M. Grabowski, and R. Camley, J. Magn. Magn. Mater. **322**, 2127 (2010).

[31] R. K. Smith, M. Grabowski, and R. Camley, J. Magn. Magn. Mater. **321**, 3472 (2009).

[32] D. Laroze, P. Vargas, C. Cortes, and G. Gutierrez, J. Magn. Magn. Mater. **320**, 1440 (2008).

[33] D. V. Vagin and O. P. Polyakov, J. Magn. Magn. Mater. **320**, 3394 (2008).

[34] L. Berger, Phys. Rev. B **54**, 9353 (1996).

[35] J. C. Slonczewski, J. Magn. Magn. Mater. **159**, L1 (1996).

[36] J. A. Katine, F. J. Albert, R. A. Buhrman, E. B. Myers, and D. C. Ralph, Phys. Rev. Lett. **84**, 3149 (2000).

[37] S. Mangin, D. Ravelosona, J. Katine, M. Carey, B. Terris, and E. E. Fullerton, Nat. Mater. **5**, 210 (2006).

[38] S. Okamoto, N. Kikuchi, M. Furuta, O. Kitakami, and T. Shimatsu, J. Phys. D **48**, 353001 (2015).

[39] T. Fal and R. Camley, Appl. Phys. Lett. **97**, 122506 (2010).

[40] J. Stohr and H. C. Siegmann, *Solid-State Sciences* (Springer, Berlin/Heidelberg, 2006), Vol. 5.

[41] E. Hairer, S. P. Norsett, and G. Wanner, *Solving Ordinary Differential Equations I. Nonstiff Problems*, 2nd ed. (Springer-Verlag, Berlin/Heidelberg, 1993).

[42] A. C. Hindmarsh, in *Scientific Computing*, edited by R. S. Stepleman *et al.*, Vol. 1 of IMACS Transactions on Scientific Computation (North-Holland, Amsterdam, 1983), pp. 55–64.

[43] M. d'Aquino, C. Serpico, and G. Miano, J. Comput. Phys. **209**, 730 (2005).

[44] R. C. Hilborn, *Chaos and Nonlinear Dynamics: An Introduction for Scientists and Engineers*, 2nd ed. (Oxford University Press on Demand, New York, 2006).

[45] Y. A. Kuznetsov, *Elements of Applied Bifurcation Theory* (Springer Science and Business Media, New York, 2013), Vol. 112.

[46] H. Ebert, Rep. Prog. Phys. **59**, 1665 (1996).

[47] A. B. Kos, T. J. Silva, and P. Kabos, Rev. Sci. Instrum. **73**, 3563 (2002).

[48] B. Kuanr, Z. Celinski, and R. Camley, Appl. Phys. Lett. **83**, 3969 (2003).

[49] A. Aharoni, J. Appl. Phys. **83**, 3432 (1998).